Modeling and Experimental Verification of a Cable-Driven Rolling Joint System Considering Preload and Friction Effect

Song Zeng, Yixin Zhang, Shaoping Wang, Giorgio Guglieri, Stefano Primatesta, and Wenjie Wu

***Abstract*—In the realm of cable-driven robotics, the cable-driven rolling joint (CDRJ) is a transformative innovation that effectively increases stiffness based on biomimicry while maintaining the robot's slim and lightweight structure. This study presents a comprehensive model of CDRJ that meticulously considers the effects of cable friction, integrating the influences of cable pretension, elastic deformation, and the frictional interaction between the cable and the pulley on the system's performance. The research delves into the distribution law of cable tension influenced by frictional forces and the consequential motion hysteresis observed during reverse rotation. An enhanced LuGre friction model is introduced to address the complexities of line contact friction between cables and pulleys. Building upon this, a dynamic model of CDRJ is established, capturing the motion characteristics throughout the process, including the discontinuous friction phenomena inherent in reverse rotation. This article culminates with the construction of an experimental prototype of a cable rolling joint system, through which the friction coefficient is determined. Experimental results corroborate the dynamic model's proficiency in simulating the motion characteristics of CDRJ, underscoring its potential for accurate tension prediction and force assessment within intricate pulley systems. Meanwhile, the generalized model of the pulley–cable system developed in this research may be applied in the fields of biomechanics, prosthetics, and bionic design, providing new insights into various cable-driven systems.**

***Index Terms*—Bionic, cable-driven rolling joint (CDRJ), friction analysis, preload, tension distribution.**

Received 21 May 2024; revised 1 September 2024; accepted 30 October 2024. Recommended by Technical Editor T. Das and Senior Editor H. Fujimoto. This work was supported in part by the National Natural Science Foundation of China under Grant U2233212 and Grant 52205299 and in part by the China Postdoctoral Science Foundation under Grant 2022M710304. *(Corresponding author: Shaoping Wang.)*

Song Zeng, Yixin Zhang, Shaoping Wang, and Wenjie Wu are with the School of Automation Science and Electrical Engineering, Beihang University, Beijing 100191, China (e-mail: song_zeng@buaa.edu.cn; zhang_yixin@buaa.edu.cn; shaopingwang@buaa.edu.cn; wuwenjie@buaa.edu.cn).

Giorgio Guglieri and Stefano Primatesta are with the Department of Mechanical and Aerospace Engineering, Politecnico di Torino, 10129 Torino, Italy (e-mail: giorgio.guglieri@polito.it; stefano.primatesta@polito.it).

Color versions of one or more figures in this article are available at https://doi.org/10.1109/TMECH.2024.3491154.

Digital Object Identifier 10.1109/TMECH.2024.3491154

I. Introduction

In the realm of modern engineering, cable-driven mechanisms are esteemed for their minimal mass, economical nature, and proficiency in transmitting power across extensive distances [1]. These mechanisms are particularly integral to the functionality of surgical robots and interactive robotic arms [2], [3]. The cable-driven rolling joint (CDRJ) is a new type of bionic motion structure that improves joint output stiffness through a tension amplification mechanism. Many scholars have proposed humanoid mechanical upper and lower limbs containing rolling joints [4], [5], [6], [7], but they are mainly structural optimization and discussion of stiffness. Nonetheless, the inherent limitations of cable rigidity and tensile strength necessitate the development of strategies to bolster operational safety and diminish the likelihood of cable failure [8]. However, the constraints imposed by the compactness of design and budgetary considerations render the incorporation of supplementary sensors for tension monitoring impractical [9]. Consequently, enhancing the precision of the system's model for tension prediction and estimation is imperative. Current models of cable and pulley systems predominantly focus on localized analyses, examining individual pulleys and cables without accounting for the overarching pulley layout's influence.

At present, many studies have done related work on the modeling of pulleys and cable bodies. Yuan et al. [10] conducted static and dynamic stiffness analyses for a long-span cable-driven mechanism, where the cable's mass and elasticity could not be disregarded. Qi et al. [11] developed motion models for flexible cables, accounting for changes in length, and carried out coupled motion analyses between cables and winches or pulleys. Peng et al. [12] introduced an efficient multibody modeling approach for cable–pulley systems with friction, introducing a variable-length cable element with movable nodes. In large-scale cable-driven systems, cable quality and deformation significantly impact system response. Commonly used cable modeling methods include the finite-element method and the absolute node coordinate method [13]. However, in miniaturized cable-driven systems, the cables employed are typically small in length and size, with the mass effect during movement being negligible [14]. Under the aforementioned cable bearing system, it basically only involves the static or dynamic deformation analysis of the cable, and there is little consideration for the friction of the cable pulley and the preload of the cable, and it is often difficult to make a more accurate evaluation of the system state.

In terms of the contact characteristics of pulleys and cables, two prevalent friction models are employed to describe the

friction between pulleys and cables. The first model is Euler's model [15], which elegantly expresses tension over the pulley or capstan as a decaying exponential function. Ju and Choo [16] introduced a parametric superelement model where cables pass through multiple pulleys based on the Euler model, primarily used for static analysis under heavy loads. The second friction model, proposed by Grashof [17], refines Euler's model by dividing the contact arc into the adhesion arc and the sliding arc [18]. In the adhesion arc, the tension remains constant, while in the sliding arc, the tension varies following the exponential function just like Euler's model. Cho et al. [19] illustrated the relevant deformation based on the Grashof model. The current cable–pulley models are analyzed by the static friction model, and the sliding friction is mainly considered. In general mechanical systems, dynamic friction models are widely used to capture more properties of the system by using additional state variables. Pennestrì et al. [20] introduced the currently widely used dynamic friction models, such as Dahl model, LuGre model, Gonthier model, etc. The LuGre model is an extension of the Dahl model, which captures the Stribeck effect and, therefore, can describe stick–slip motion. The LuGre model contains only a few parameters and can, therefore, be easily matched to experimental data [21].

In this article, we conduct a detailed study of the design analysis and cable system modeling methods of CDRJ and illustrate three contributions. First, a rolling joint mechanism was analyzed, the kinematic and dynamic models satisfying the rolling joint were solved, and the relationship between joint torque and cable system tension was deduced. Second, a novel pulley and cable system modeling method is proposed, which can simplify the complex pulley system and iteratively solve the tension value of any node and element of the cable system. In addition, the improved LuGre sliding friction model and the rolling friction model were used to solve the overall friction problem of the cable–pulley line contact. This model can accurately reflect the changes in cable tension through the pulley. On this basis, a rolling joint experimental platform was established to verify the model.

The rest of this article is organized as follows. Section II introduces the proposed bilateral conjugate rolling joint. Section III introduces the nodal element cable tension model, considering the friction effect and preload. Section IV deeply analyzes the impact of rolling friction and sliding friction models on the system. Section V establishes a rolling joint experimental platform to validate our model simulation results. Finally, Section VI concludes this article.

II. Analysis of the CDRJ System

A. Introduction to Rolling Joints and Cable Systems

In pursuit of augmented joint torque and heightened energy efficiency without surplus motors, recent scholarly endeavors have introduced a rolling joint structure; it is widely used in cable-driven elbow joints and knee joints of upper and lower limbs [7], [22]. By leveraging the opposing characteristics of cables, it becomes possible to ensure that as one side of the cable changes length during movement, the other side adjusts accordingly. This article proposes an implementation method of rolling joints based on conjugate gears, as shown in Fig. 1(a), which can improve the overall stiffness and operational stability while ensuring pure rolling characteristics. At the same time, a symmetrical pulley cable layout method is proposed, as shown in Fig. 1(b).

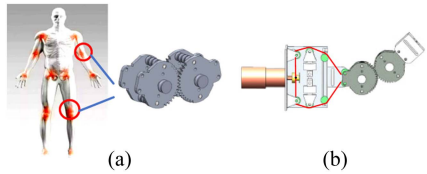

Fig. 1. (a) Conjugate gear rolling joint. (b) Pulley layout system.

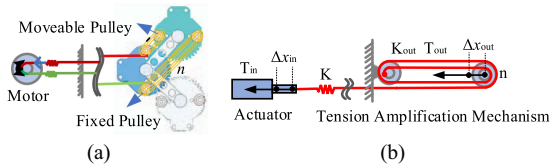

Fig. 2. (a) Tension amplification principle. (b) Rolling joint mechanism. n is the number of cable windings, Δx_{out} is the cable length change of joint, Δx_{in} is the cable length change of the winch, T_{in} is the tension of one single cable, T_{out} is the joint output tension, K_{cable} is the stiffness of the one single cable, and K_{out} is the joint output stiffness.

The pulley's symmetry ensures that elongated and contracted cables maintain the same length and speed. The rolling joint mainly consists of two parts, which pass through the independent cable systems of the upper and lower fixed pulleys and the movable pulley, respectively, and the first ends of both the cable systems are fixed at the edge of the motor winch, and the ends are fixed at the rolling joint. When the upper cable length decreases, the lower cable length correspondingly increases, while the joint angle changes; in this process, the dynamic pulley position changes with the change of joint angle, while the number of cables turns wound on the dynamic fixed pulley will affect the overall operating speed and efficiency. Furthermore, cables with varying number of turns can enhance the force on the pulley, creating a combined effect akin to that of both the movable and static pulleys. As depicted in Fig. 2, these parameters adhere to the following relationship:

$$\begin{aligned} \Delta x_{\text{out}} &= \Delta x_{\text{in}}/n \\ T_{\text{out}} &= nT_{\text{in}} \\ K_{\text{cable}} &= T_{\text{in}}/\Delta x_{\text{in}} \\ K_{\text{out}} &= T_{\text{out}}/\Delta x_{\text{out}} = n^2 T_{\text{in}} \Delta x_{\text{in}} = n^2 K_{\text{cable}}. \end{aligned} \tag{1}$$

B. Joint Kinematics

As shown in Fig. 3(a), we can get the overall relationship between the rolling joint motion angle and the cable length. When θ is zero, l_{up} and l_{down} have the same length as nd.

According to the simplified winding method [see Fig. 3(b)], the following relationship can be obtained:

$$\begin{aligned} l_{\text{up}} &= n(d - w\sin\theta) \\ l_{\text{down}} &= n(d + w\sin\theta) \\ \Delta l &= \Delta l_{\text{up}} = -\Delta l_{\text{down}} = nw\sin\theta \end{aligned}$$

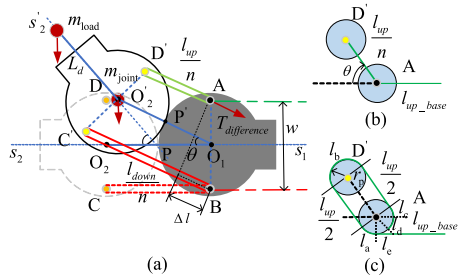

Fig. 3. (a) Joint motion analysis, l_{up} is the total length of the upper cables, l_{down} is the total length of the lower cables, Δl is the change in length of the upper and lower sets of cables, d is the diameter of the rolling surface, w is the installation width of the pulley, θ is the link angle, n is the number of winding turns. (b) Cable length analysis ignoring the pulley radius, l_{up_base} is the length of the remaining part except for the cable of the pulley. (c) Cable length analysis considering the pulley radius, r_p is the pulley radius, and l_a, l_b, l_c, l_d, and l_e are the lengths of the parts in contact with the pulley, respectively.

$$\theta = \arcsin\left(\frac{\Delta l}{nw}\right). \tag{2}$$

As shown in Fig. 3(c), considering the size of the guide pulley and assuming an even number of n (here, $n = 2$), the actual wire length l_{total} is

$$\begin{aligned} l_{total} &= l_{up\_base} + l_a + l_{up}/2 + l_b + l_{up}/2 + l_c + l_d \\ &= l_{up\_base} + l_{up} + (2\pi r_p - l_e). \end{aligned} \tag{3}$$

When the bending angle θ changes, only the lengths l_a and l_c adjust accordingly, while the other lengths remain constant. With an even number of turns, the actual wire length, l_{total}, is solely dependent on l_{left}, mirroring the movement of the simplified winding. The elongation and contraction of the cables at both the ends are symmetric. In principle, a pretensioning mechanism is not necessary to prevent cable slack, but the total cable length must be adjusted to establish the desired cable pretensioning force.

C. Joint Dynamics

Establishing a dynamic model for the cable can be more complex, primarily due to its stiffness. To simplify the analysis process in cable-driven manipulator control and modeling, cables are often treated as rigid, neglecting their mass and deformation, as seen in the literature [5], [23]. Given the relatively small scale of the cable-driven joint system and the limited inner diameter and length of the cable used, the cable's mass is negligible compared to the joint and the load. Therefore, only the impact of its deformation is considered.

Following principles from Newtonian and Lagrangian mechanics, the fundamental dynamic model for the mechanical arm joint is as follows:

$$\tau = D(q)\ddot{q} + C(q,\dot{q}) + G(q) \tag{4}$$

where τ is the joint moment, $D(q)$ is the $n\times n$ mass matrix of the joint, $C(q,\dot{q})$ are $n\times 1$ centrifugal force and Coriolis force vectors, and $G(q)$ is the gravity vector of $n\times 1$.

As depicted in Fig. 3(a), the pure rolling meshing process of the conjugate gear leads to the joint's angular velocity being twice the rotational angular velocity of the gear. This design approach effectively expands the joint's range of motion within the limited rotation range of the gear. With a load, the joint can achieve a range of motion within 45°, and the end load can have a motion range of 180°. Assuming that the rolling components can be approximated as circular and disregarding the masses and radius of the pulley and the cable, as well as the deformations and frictions of the end cable, the joint dynamics can be described using the Lagrange dynamic equation. The rotational kinetic energy and moment of inertia can be determined using the following formulas:

$$K_{joint} = \frac{1}{2}I_{o_1}\dot{\theta}^2 + \frac{1}{2}I_{o_2}(2\dot{\theta})^2 = 3m_{joint}\dot{\theta}^2R^2. \tag{5}$$

When the initial horizontal position is considered as the zero point of potential energy, the joint's potential energy can be calculated as

$$P_{joint} = m_{joint}g\cdot(2R)\sin\theta. \tag{6}$$

Likewise, the kinetic energy and the potential energy of the end load can be determined as follows, with L_d representing the distance between the end load and the center of the joint:

$$K_{load} = \left(\frac{5}{2}{L_d}^2 + 2R^2 + 2L_dR\cos\theta\right)m_{load}\dot{\theta}^2 \tag{7}$$

$$P_{load} = m_{load}g(2R\sin\theta + L_d\sin 2\theta). \tag{8}$$

By substituting into the Lagrange kinetic equation, the driving moment τ_θ of the joint is equal to the product of the tension difference T between the upper and lower sets of cables and the moment arm

$$\begin{aligned} &\left[6m_{joint}R^2+(5{L_d}^2+4R^2+4L_dR\cos\theta)m_{load}\right]\ddot{\theta}-2L_dR\sin\theta \\ &m_{load}\dot{\theta}^2+2g\left[m_{joint}R\cos\theta+m_{load}(R\cos\theta+L_d\cos 2\theta)\right]=\tau_\theta. \end{aligned} \tag{9}$$

Considering that the tension difference at the tension amplification pulley forms the active moment driving the joint, it can be expressed as

$$T_{difference}\frac{w}{2}\cos\theta = \tau_\theta. \tag{10}$$

Therefore, it can be seen from (10) that the output torque of the joint is related to the tension difference between the upper and lower cable systems and the angle of the joint. The tension difference between the upper and lower cables can be solved inversely through the dynamic equation in (9).

III. Modeling of the Cable–Pulley System

Despite the diverse layouts and applications of cable-driven systems, their fundamental components primarily consist of winches, cables, pulleys, and fixed anchor points. As a result, leveraging the node element concept from the finite-element method allows for the simplification and solution of complex systems through iterative methods [24]. The current pulley node finite-element analysis scenarios are mainly for cranes, transmission lines, parachutes, and other cable bearing systems; most of the existing models are analyzed only for the static mechanics, without considering the dynamic problems. At present, this kind of sliding cable system does not involve the cable preload problem.

Due to the tension amplification joint in the CDRJ system, the number of pulleys contained in the system is far more than that

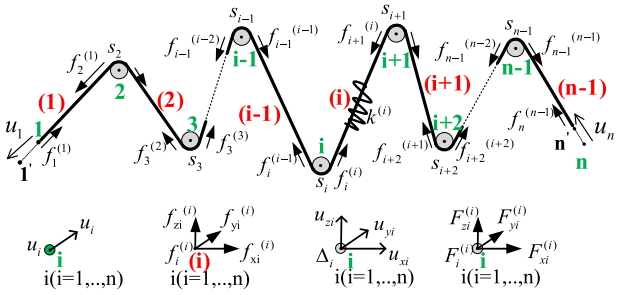

Fig. 4. System node element and tension transfer model.

of the traditional pulley system. In order to comprehensively analyze the influence of the overall pulley–cable system, the finite-element iteration method can more accurately capture the complex mechanical and kinematic characteristics of the system. Especially, in the case of multiple factors, such as cable length change, preload, tension, friction, and pulley system, the finite-element iteration method provides more refined simulation results through segmented simulation and stepwise approximation. To the best of our knowledge, this article is the first to incorporate a finite-element iterative method applied to a similar rolling joint cable-driven analysis scenario.

Fig. 4 illustrates the elastic deformation of a continuous cable passing through multiple intermediate pulleys, which are affixed to brackets. The entire system comprises n nodes, $n-1$ cables, and $n-2$ pulleys. The cable can transition from one side of the pulley to the other due to pulley rotation, cable sliding friction, or a combination of both. It can be assumed that when the cable's length between two nodes greatly exceeds the pulley's winding length, cable elongation primarily concentrates in the middle section of the cable (i) and is influenced by both the preceding and succeeding pulleys. The transfer length of the pulley is denoted as s_i $(i = 2, \ldots, n-1)$, with $s_1 = s_n = 0$. The entire pulley system may consist of both the fixed and movable pulleys, resulting in node displacement u_i $(i = 1, 2, \ldots, n)$, particularly when the adjacent pulley is a fixed pulley or a fixed anchor point, where $u_i = 0$.

During the model construction and experiments, the following assumptions were made to simplify the system structure and analysis process.

1) The cable exhibits linear elongation under small deformations.
2) The modulus of elasticity and the cross-sectional area of the cable change negligibly during the motion.
3) The mass of the cable is negligible and, hence, not considered in the calculations.

A. Cable Element and Pulley Node Force Modeling

Simultaneously, the cable forces acting on each node are recorded as $f_i^{(i)}$, where the subscript i denotes the ith node, and the superscript (i) designates the ith section of the cable. Many prior studies [25], [26] have developed dynamic models for cable-actuated robotic manipulators featuring elastic cables. In these models, the elastic cable connecting two pulleys is typically represented by a linear spring. However, linear springs can apply both the tensile and compressive forces, which may not accurately reflect the actual properties of tendons. In this study, we propose a method for modeling unidirectional forces in tendons.

Fig. 4 illustrates the process of generating cable tension through cable deformation and movement between adjacent pulley blocks. Let us assume that the deformation resulting from the initial preload force on each section is denoted as $u_{0,i} + s_{0,i}$, and the corresponding tension is $t_{0,i} = k^{(i)}(u_{0,i} + s_{0,i} - u_{0,i+1} - s_{0,i+1})$. When applying the preload force to maintain the joint in its initial position, where $u_i = 0$ $(i = 1, 2, \ldots, n)$, only the pulley segment experiences minor displacements. These cumulative small displacements are subsequently fixedly constrained by the end anchor points.

If the positive rotation of the pulley is defined as the counterclockwise rotation of the pulley, then for a small angle of rotation of the pulley, the magnitude of the tension in the ith cable is t_i

$$t_i = \Gamma^+\{t_{0,i} - k^{(i)}(u_i + s_i - u_{i+1} - s_{i+1})\}. \tag{11}$$

It can be noted that $\Gamma^+(x)$ returns its value only when the argument is positive. Otherwise, $\Gamma^+(x)$ gives zero value.

Since the cable can only take axial tension, the forces on both the sides of the same cable unit are equal in value but opposite in direction; the relationship between cable deformation and force can be established as

$$\begin{Bmatrix} f_i^{(i)} \\ f_{i+1}^{(i)} \end{Bmatrix} = \begin{bmatrix} k^{(i)} & -k^{(i)} \\ -k^{(i)} & k^{(i)} \end{bmatrix} \begin{Bmatrix} u_{0,i} + s_{0,i} - u_i - s_i \\ u_{0,i+1} + s_{0,i+1} - u_{i+1} - s_{i+1} \end{Bmatrix}. \tag{12}$$

Substituting the expression of $t_{0,i}$ into (12) and deforming the matrix yields

$$\begin{Bmatrix} f_i^{(i)} \\ f_{i+1}^{(i)} \end{Bmatrix} = \begin{Bmatrix} t_{0,i}^{(i)} \\ t_{0,i+1}^{(i)} \end{Bmatrix} - k^{(i)} \begin{bmatrix} 1 & -1 & 1 & -1 \\ -1 & 1 & -1 & 1 \end{bmatrix} \begin{Bmatrix} u_i \\ u_{i+1} \\ s_i \\ s_{i+1} \end{Bmatrix} \tag{13}$$

where $f_i^{(i)}$, u_i,s_i, and $f_{i+1}^{(i)}$,u_{i+1},s_{i+1} are the axial force, displacement, and the wrap length at nodes i and $i+1$, respectively. The nominal stiffness of the subelement $k^{(i)}$ is defined as

$$k^{(i)} = \frac{E^{(i)} A^{(i)}}{L^{(i)}} \tag{14}$$

where $E^{(i)}$, $A^{(i)}$, and $L^{(i)}$ are Young's modulus, cross-sectional area, and length of the subelement, respectively. If the modulus of elasticity and the cross-sectional area of the cable change negligibly during the motion, when the length of the cable between adjacent nodes changes, the stiffness of each cable segment also changes.

Transforming nodal forces and displacements from local subelement coordinates to global coordinates gives

$$\begin{Bmatrix} t_{0,i}^{(i)} - f_i^{(i)} \\ t_{0,i+1}^{(i)} - f_{i+1}^{(i)} \end{Bmatrix} = \begin{bmatrix} \boldsymbol{\lambda}^{(i)} & 0 \\ 0 & \boldsymbol{\lambda}^{(i)} \end{bmatrix} \begin{Bmatrix} \boldsymbol{T}_{0,i}^{(i)} - \boldsymbol{F}_i^{(i)} \\ \boldsymbol{T}_{0,i+1}^{(i)} - \boldsymbol{F}_{i+1}^{(i)} \end{Bmatrix} \tag{15}$$

$$\begin{Bmatrix} u_i \\ u_{i+1} \\ s_i \\ s_{i+1} \end{Bmatrix} = \begin{bmatrix} \boldsymbol{\lambda}^{(i)} & 0 & 0 & 0 \\ 0 & \boldsymbol{\lambda}^{(i)} & 0 & 0 \\ 0 & 0 & 1 & 0 \\ 0 & 0 & 0 & 1 \end{bmatrix} \begin{Bmatrix} \Delta_i \\ \Delta_{i+1} \\ s_i \\ s_{i+1} \end{Bmatrix} \tag{16}$$

where $\{\boldsymbol{F}_i^{(i)}\}$, $\{\boldsymbol{F}_{i+1}^{(i)}\}$ and $\{\Delta_i\}$, $\{\Delta_{i+1}\}$ are the nodal force and the displacement vectors at the global coordinate system, respectively, as shown in Fig. 4 defined by (17) shown at the

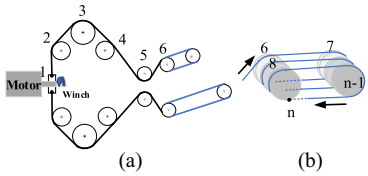

Fig. 5. (a) Simplified schematic diagram of a CDRJ system. (b) Schematic diagram of tension amplification mechanism winding.

bottom of this page, where $\boldsymbol{\lambda}^{(i)}$ is the transformation coefficient corresponding to the local coordinate system to the global coordinate system, which corresponds to the change of the node's displacement u_i along the direction of cable motion and the global displacement Δ_i, while the cable length s_i transferred by the pulley wrap is always along the direction of cable motion.

By substituting (15) and (16) into (13) and using the orthogonal property of the transformation matrix, the following element matrix equation is obtained:

$$\begin{Bmatrix} \boldsymbol{T}_i^{(i)} - \boldsymbol{F}_i^{(i)} \\ \boldsymbol{T}_{i+1}^{(i)} - \boldsymbol{F}_{i+1}^{(i)} \end{Bmatrix}_{6\times1} = \begin{bmatrix} \mathbf{k}_{\Delta\Delta}^{(i)} & -\mathbf{k}_{\Delta\Delta}^{(i)} & \mathbf{k}_{\Delta s}^{(i)} & -\mathbf{k}_{\Delta s}^{(i)} \\ -\mathbf{k}_{\Delta\Delta}^{(i)} & \mathbf{k}_{\Delta\Delta}^{(i)} & -\mathbf{k}_{\Delta s}^{(i)} & \mathbf{k}_{\Delta s}^{(i)} \end{bmatrix}_{6\times8} \begin{Bmatrix} \Delta_i \\ \Delta_{i+1} \\ s_i \\ s_{i+1} \end{Bmatrix}_{8\times1} \tag{18}$$

$$\left[\mathbf{k}_{\Delta\Delta}^{(i)}\right]_{3\times3} = k^{(i)}\left[\boldsymbol{\lambda}^{(i)}\right]^{\mathrm{T}}\left[\boldsymbol{\lambda}^{(i)}\right], \left[\mathbf{k}_{\Delta s}^{(i)}\right]_{3\times1} = k^{(i)}\left[\boldsymbol{\lambda}^{(i)}\right]^{\mathrm{T}}. \tag{19}$$

Considering the force equilibrium conditions at each node, the following equation for the node element can be obtained:

$$\{\boldsymbol{T}-\boldsymbol{F}\}_{3n\times1} = [\mathbf{K}_{\Delta\Delta} \quad \mathbf{K}_{\Delta s}]_{3n\times(4n-2)} \begin{Bmatrix} \boldsymbol{\Delta} \\ \mathbf{S} \end{Bmatrix}_{(4n-2)\times1} \tag{20}$$

where $\{\boldsymbol{T}-\boldsymbol{F}\}_{3n\times1}$ and $\{\boldsymbol{\Delta}\}_{3n\times1}$ are the conventional nodal forces and displacements of the cable system, $[\mathbf{K}_{\Delta\Delta}]_{3n\times3n}$ and $[\mathbf{K}_{\Delta s}]_{3n\times(n-2)}$, which are, respectively, assembled from (18) and (19), and $\{\mathbf{S}\}_{(n-2)\times1}$ is

$$\{\mathbf{S}\}_{(n-2)\times1} = [s_2 \quad s_3 \quad \ldots \quad s_{n-2} \quad s_{n-1}]^{\mathrm{T}}. \tag{21}$$

The system consists of two independent cable systems, as illustrated in Fig. 5(a). At the rolling joint, the cable is wound multiple times through a tension amplification mechanism, as shown in Fig. 5(b). By integrating the established tension distribution and kinematic models, the relationship between the elastic force of each cable element, pulley node displacement, and cable length changes can be determined.

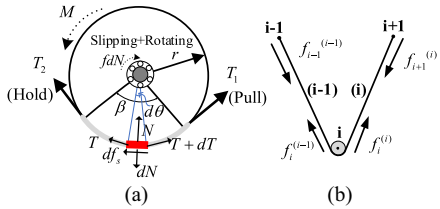

Fig. 6. (a) Basic principles of cable and pulley winding. M is the driven torque, T_1 is the tension of the cable pull end, T_2 is the tension of the cable hold end, r is the radius of the pulley, and β is the transmission wrap angle. (b) Cable passes through the node model on both sides of the pulley.

The rolling joint system discussed represents a more complex configuration within cable-driven mechanisms. Here, a single motor drives two independently pretensioned cable systems, with pulleys introducing significant variations in cable segment length. The proposed model is applicable to most of the existing cable-driven mechanisms. For example, in traditional hoisting systems without pretension, the model can be applied by setting pretension to zero. Similarly, in conventional serial or parallel cable-driven robots, where each motor typically drives a single cable and the guiding pulleys are fixed, the model can be simplified to a scenario with a single pretension and zero pulley node displacement. Consequently, this model is broadly applicable to mechanisms incorporating pulley–cable systems, such as cable-driven dexterous hands, robotic arms, and miniature surgical robots.

B. Cable–Pulley Tension Transfer

When tension is transferred through the pulley, relative motion occurs between the cable and the pulley. Friction influences this process, resulting in a disparity in tension on both the sides; the actual friction comes from the sliding friction between the cables and pulleys and the rotational friction of the bearings. The difference in tension is quantified by the transfer coefficient η, as depicted in Fig. 6(a)

$$T_2 = \eta T_1. \tag{22}$$

Consider the force at node i, where cable elements $i-1$ and i are connected to the ith pulley, as shown in Fig. 6(b). Substituting into (13), the nodal axial force can be expressed as

$$\begin{Bmatrix} f_j^{(j)} \\ f_{j+1}^{(j)} \end{Bmatrix} = \begin{Bmatrix} t_{0,j}^{(j)} \\ t_{0,j+1}^{(j)} \end{Bmatrix} - k^{(i)} \begin{bmatrix} \boldsymbol{\lambda}^{(j)} & -\boldsymbol{\lambda}^{(j)} & 1 & -1 \\ -\boldsymbol{\lambda}^{(j)} & \boldsymbol{\lambda}^{(j)} & -1 & 1 \end{bmatrix} \begin{Bmatrix} \Delta_j \\ \Delta_{j+1} \\ s_j \\ s_{j+1} \end{Bmatrix} \tag{23}$$

$$\begin{cases} \left\{\boldsymbol{F}_i^{(i)}\right\} = \left[f_{xi}^{(i)} \quad f_{yi}^{(i)} \quad f_{zi}^{(i)}\right]^{\mathrm{T}}, \left\{\boldsymbol{F}_{i+1}^{(i)}\right\} = \left[f_{xi+1}^{(i)} \quad f_{yi+1}^{(i)} \quad f_{zi+1}^{(i)}\right]^{\mathrm{T}} \\ \left\{\boldsymbol{T}_i^{(i)}\right\} = \left[t_{0,xi}^{(i)} \quad t_{0,yi}^{(i)} \quad t_{0,zi}^{(i)}\right]^{\mathrm{T}}, \left\{\boldsymbol{T}_{i+1}^{(i)}\right\} = \left[t_{0,xi+1}^{(i)} \quad t_{0,yi+1}^{(i)} \quad t_{0,zi+1}^{(i)}\right]^{\mathrm{T}} \\ \{\Delta_i\} = \left[u_{xi} \quad u_{yi} \quad u_{zi}\right]^{\mathrm{T}}, \{\Delta_{i+1}\} = \left[u_{xi+1} \quad u_{yi+1} \quad u_{zi+1}\right]^{\mathrm{T}} \\ \left[\boldsymbol{\lambda}^{(i)}\right] = \left[\lambda_x^{(i)} \quad \lambda_y^{(i)} \quad \lambda_z^{(i)}\right] \\ \lambda_x^{(i)} = (x_{i+1}-x_i)/L^{(i)}, \lambda_y^{(i)} = (y_{i+1}-y_i)/L^{(i)}, \lambda_z^{(i)} = (z_{i+1}-z_i)/L^{(i)} \end{cases} \tag{17}$$

where $j = i$ and $i-1$, corresponding to two adjacent cable elements, respectively.

Based on (22), the axial force relationship of the two cable elements at node i can be expressed as

$$f_i^{(i)} = -\eta_i f_i^{(i-1)} \tag{24}$$

where the negative sign results from the force convention in the cable element, and η_i depends on the coefficient of friction and the contact angle at the pulley. Substituting $f_i^{(i)}$ and $f_i^{(i-1)}$ in (23) into (24) gives

$$\left[t_{0,i}^{(i)} + \eta_i t_{0,i}^{(i-1)}\right] = \begin{bmatrix} -\eta_i \mathbf{k}_{s\Delta}^{(i-1)} & \eta_i \mathbf{k}_{s\Delta}^{(i-1)} + \mathbf{k}_{s\Delta}^{(i)} & -\mathbf{k}_{s\Delta}^{(i)} \\ -\eta_i k^{(i-1)} & \eta_i k^{(i-1)} + k^{(i)} & -k^{(i)} \end{bmatrix} \times \left[\Delta_{i-1} \quad \Delta_i \quad \Delta_{i+1} \quad s_{i-1} \quad s_i \quad s_{i+1}\right]^{\mathrm{T}} \tag{25}$$

with

$$\left[\mathbf{k}_{s\Delta}^{(i)}\right] = k^{(i)}\left[\boldsymbol{\lambda}^{(i)}\right].$$

Summating (25) for $i = 2$ to n–1 gives

$$\{\mathbf{T}_0\}_{(n-2)\times 1} = [\mathbf{K}_{s\Delta} \quad \mathbf{K}_{ss}]_{(n-2)\times(4n-2)} \begin{Bmatrix} \boldsymbol{\Delta} \\ \mathbf{S} \end{Bmatrix}_{(4n-2)\times 1}. \tag{26}$$

As result, (26) defines the relationship between node displacement and pulley motion that is satisfied by the cable passing through all the pulleys in the system. The specific expression of the defined stiffness coefficient can be found in the Appendix.

Synthesizing the tension transfer relationship between the cable element and both the sides of the pulley node, (27) gives the final relationship between the general nodal displacements and forces:

$$\begin{Bmatrix} \mathbf{T} - \mathbf{F} \\ \mathbf{T}_0 \end{Bmatrix}_{(4n-2)\times 1} = [\mathbf{K}]_{(4n-2)\times(4n-2)} \begin{Bmatrix} \boldsymbol{\Delta} \\ \mathbf{S} \end{Bmatrix}_{(4n-2)\times 1} \tag{27}$$

$$[\mathbf{K}] = \begin{bmatrix} \mathbf{K}_{\Delta\Delta} & \mathbf{K}_{\Delta s} \\ \mathbf{K}_{s\Delta} & \mathbf{K}_{ss} \end{bmatrix}. \tag{28}$$

Thus, through the creation of an iterative equation, it becomes possible to deduce the deformation of the cable and the tension of each cable when the tension at any cable position, the preload force, and the end cable's movement displacement are known.

At the same time, it can be seen from (27) and (28) that with the presence of friction between the cable and the pulley, the stiffness matrix $[\mathbf{K}]$ is generally unsymmetrical. The specific result expression of $\mathbf{K}_{\Delta\Delta}$,$\mathbf{K}_{\Delta s}$,$\mathbf{K}_{s\Delta}$, and $\mathbf{K}_{ss}$ is reported in the Appendix. This matrix will become symmetrical if the frictional effect is negligible since $[\mathbf{K}_{\Delta s}] = [\mathbf{K}_{s\Delta}]^{\mathrm{T}}$, when $\eta = 1$.

IV. Friction Model Considering Sliding and Rolling Contact

Classical Euler's formula assumes that the pulley remains fixed and does not rotate, causing the cable to contact all the areas of the winch edge, resulting in pure sliding. In this case, the friction loss reaches the maximum value, and the transfer coefficient reaches the minimum value, as shown in Fig. 7(b). However, when the central pulley can rotate, the area where sliding friction occurs between the cable and the edge of the pulley gradually decreases due to the presence of rolling bearings. Ideally, there is no slippage between the cable and the pulley, causing friction loss in the bearing motion, and the transmission coefficient reaches the maximum value, as shown in Fig. 7(c). This article comprehensively considers the friction loss of the rolling bearing and the sliding friction caused by the cable–pulley contact and evaluates the tension transfer coefficient.

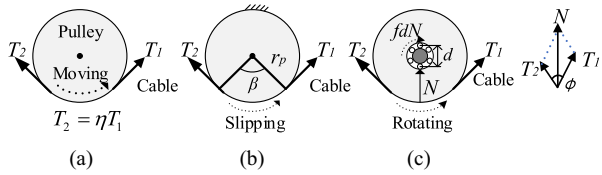

Fig. 7. Different cable–pulley friction model. (a) Tension transmission. (b) Pure sliding. (c) Pure rotating.

A. Modeling With Sliding Friction

Consider a pulley fixed at the ground and a tendon around it, as shown in Fig. 6(a), where an end of the tendon is pulled with tension T_1, while the other end is held with tension T_2.When impending motion, a differential element of the tendon is subject to two tensions $T + dT$ and T on both the sides, the normal force dN, and the friction $d\ f_s = \mu_c\ dN$, where μ_c is the coefficient of Columb friction. Force equilibrium on tangential and normal components yields

$$\frac{dT}{T} = -\mu_c d\theta \mathrm{sgn}(v) \rightarrow \int_{T_1}^{T} \frac{dT}{T} = -\int_0^{\theta} \mu_c d\theta \mathrm{sgn}(v) \tag{29}$$

$$T(\theta) = T_1 e^{-\mu_c \theta \mathrm{sgn}(v)}, 0 \le \theta \le \beta \tag{30}$$

where β is the contact angle. The friction force generated by the sliding part is

$$f_s = T_1 - T(\theta) = T_1(1 - e^{-\mu_c \theta \mathrm{sgn}(v)}). \tag{31}$$

When there is no rolling friction, the pulley is fixed and does not rotate. The passive holding tension T_2 is completely determined by the active pulling tension T_1, the friction coefficient μ_c, and the contact angle β. The amount of tension loss from T_1 to T_2 is due to the friction force f_s, applied along the path of the contact

$$\eta_s = e^{-\mu_c \beta \mathrm{sgn}(v)}. \tag{32}$$

The cable–pulley friction model obtained by (31) does not consider the case that the relative velocity is equal to zero. When the direction of velocity changes, the friction is discontinuous. It cannot deal with the friction changes during the reverse motion of the joint. LuGre [21] model is a dynamic friction model, which can more truly describe the change of friction

$$\begin{cases} f = \sigma_0 z + \sigma_1 \dot{z} + \sigma_2 v \\ \dot{z} = v - \frac{\sigma_0 |v|}{g(v)} z \\ g(v) = f_c + (f_s - f_c) e^{-(v/v_s)^2}. \end{cases} \tag{33}$$

Equation (33) is the basic expression of the LuGre model, where f is the friction force and z is the state variable representing the average bristle deflection. v is the relative velocity

of the two contact surfaces. This function simulates the Stribeck effect and $g(v) > 0$. σ_0, σ_1, and σ_2 are elastic stiffness, damping, and viscous friction parameters, respectively. f_c and f_s are the Coulomb friction and the maximum static friction, respectively. v_s is the Stribeck speed.

The cable and the pulley are in linear contact, and the calculation of friction needs to be integrated along the pulley path. To extend the LuGre model to the line contact dynamic friction model, some improvements are made to the LuGre model given in (33). The basic idea is to take the friction as a whole and combine the cable–pulley static friction model to get the equivalent LuGre model parameters, thus extending the LuGre friction model into a dynamic friction model suitable for calculating the cable–pulley friction. Inspired by Li et al. [27], we have made some improvements to convert static friction into the dynamic friction process.

Improvement 1: Combined with (30), the equivalent Coulomb friction is obtained, and a sufficiently small damping term ε is added to avoid numerical problems

$$f_c = T_{\text{in}} - T_{\text{out}} = T_{\text{in}}(1 - e^{-\mu_c \theta \text{sgn}(v)}) + \varepsilon. \tag{34}$$

Improvement 2: Because the static friction is difficult to obtain, the friction coefficient is determined by the materials of the two contact surfaces, and the equivalent maximum static friction is defined as follows:

$$f_s = \frac{\mu_s}{\mu_c} f_c \tag{35}$$

where μ_s is the static friction coefficient and μ_c is the Coulomb friction coefficient.

Considering the steady-state sliding, the system satisfies $\dot{z} = 0$, and $z_0 = \frac{g(v)}{\sigma_0}\ \text{sgn}(v)$. When ignoring viscous friction, there is

$$\begin{aligned} f &= \sigma_0 z_0 = g(v)\text{sgn}(v) \\ &= [f_c + (\mu_s/\mu_c - 1) f_c e^{-(v/v_s)^2})]\text{sgn}(v). \end{aligned} \tag{36}$$

Then, we can get

$$\eta_d = 1 - (1 - e^{-\mu_c \theta \text{sgn}(v)} + \varepsilon)[1 + \left(\frac{\mu_s}{\mu_c} - 1\right) e^{-(v/v_s)^2}]. \tag{37}$$

The parameters θ and v are related to the pulley–cable configuration and the motor drive, with a focus on the LuGre model parameters: μ_s, μ_c, and v_s. Given that the pulley–cable systems typically utilize metallic cables and operate at relatively low velocities, the ranges for μ_s and μ_c are identified as [0.2, 0.4] and [0.1, 0.3], respectively, while v_s is generally below 0.1 mm/s. The sensitivity analysis of these parameters, as illustrated in Fig. 8, indicates that within these specified ranges, the dynamic tension transmission coefficient exhibits an approximately linear relationship with parameter variations, consistently remaining above 0.8. This analysis demonstrates that despite the influence of the LuGre model parameters μ_s, μ_c, and v_s, the model remains robust and reliable, thereby validating its applicability and effectiveness in accurately representing the friction dynamics in pulley–cable systems.

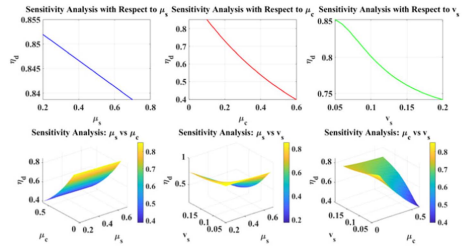

Fig. 8. Sensitivity analysis of main parameters of the dynamic transfer coefficient.

B. Modeling With Rolling Friction

When there is no sliding friction, the following equation is valid:

$$N(T_1, T_2, \phi) = |T_1 + T_2| = \sqrt{T_1^2 + T_2^2 + 2T_1 T_2 \cos\phi} \tag{38}$$

$$(T_1 - T_2) r_p = f_d d N. \tag{39}$$

It can be seen from Fig. 7(c) that $\phi = \pi - \beta$, and set $\alpha = r_p/(f_d d)$; then, we substitute these two parameters into (38) and (39)

$$(\alpha^2 - 1)\eta^2 - 2(\alpha^2 - \cos\beta)\eta + \alpha^2 - 1 = 0 \tag{40}$$

$$\eta_r = \frac{\alpha^2 - \cos\beta - \sqrt{(1 - \cos\beta)(2\alpha^2 - \cos\beta - 1)}}{\alpha^2 - 1}. \tag{41}$$

When considering both the sliding friction between the pulley and the cable and the rolling friction of the bearing, the following moment balance equation is satisfied:

$$(T_1 - T_2) r_p = f_d d N + f_s r_p. \tag{42}$$

The actual tension transfer coefficient η satisfies

$$\eta_r \le \eta < \eta_d. \tag{43}$$

Different weighting factors are assigned to different friction effects; define ρ as the sliding friction influence coefficient. Define $\eta = \rho\eta_d + (1 - \rho)\eta_r$; different ρ values can be selected to simulate changes in friction coefficient according to different stress states.

C. Influence of Different Friction Effects

The effects of rolling friction and sliding friction on the tension transmission of the system have been discussed. In the simulation, the preload force of the upper and lower cable systems is set to 20 N. When the system is completely influenced by sliding friction, the coefficient ρ is set to 1. Conversely, when the system is entirely affected by rolling friction, the coefficient ρ is adjusted to 0.

As depicted in Fig. 9, the friction force exerts a substantial impact on the tension of the cable. When solely considering the bearing rolling friction, a notable disparity in tension between the upper and lower cable systems is observed, signifying the potential for a heightened driving force to be generated as the joint transitions between states. Conversely, considering only sliding friction, the tension in both the upper and lower cable systems diminishes, with a more pronounced loss of tension in the upper cable, highlighting a significant reduction in driving

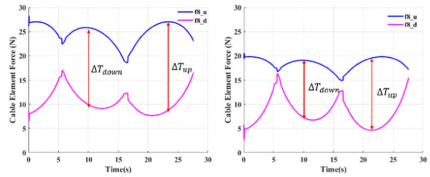

Fig. 9. Different friction effects. (a) Simple rolling friction ($\rho = 0$). (b) Simple sliding friction ($\rho = 1$). ΔT_{down} is the tension difference for downward movement and ΔT_{up} is the tension difference for upward movement.

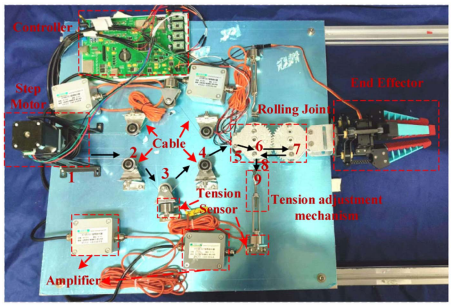

Fig. 10. Experimental platform. The cable system is symmetrically arranged vertically, and the black arrows are used to indicate the cable winding order.

efficiency and force attributable to the influence of sliding friction. Furthermore, distinct driving forces are necessitated for the upward and downward motion of the joints, with a greater variance in tension observed during upward movement due to the necessity of overcoming the gravitational forces acting on the joints and their extremities. In contrast, the gravitational component serves as the dominant driving force during downward motion. Thus, it is imperative to establish an appropriate sliding friction factor, denoted as ρ, in accordance with the specific operational conditions.

V. Simulation and Experimental Verification

A. Experimental Setup

The experimental platform is composed of two symmetrical cable–pulley systems at the top and the bottom, featuring nine nodes including seven pulley nodes and two end anchor nodes, as illustrated in Fig. 10. Two 0.2-mm 304 stainless steel stranded wires were used in the experiment. The elastic modulus of the cable is about 200 GPa, the mass of the joint itself is about 0.2 kg, and the mass of the end effector load is about 0.3 kg. At the cable's end, a pretensioning device is connected, allowing for the adjustment of the cable tension by rotating the end screws. The preload force can be modified when stationary, with tension measured by the tension sensor. The cable on the experimental platform is wound around the tension amplifying pulley of the rolling joint after passing through four guiding pulleys from the motor end, where the pulleys are made of stainless steel, and the pulley dimensions, bearing diameters, and pulley wrap angles can be obtained from Table I. Li et al. [27] have a similar configuration of cable–pulley contact; the LuGre parameters are

TABLE I
Pulley Parameters

Pulley	2	3	4	5	6	7	8
Diameter (mm)	22	22	22	13	9	9	9
Bearing diameter (mm)	10	10	10	6	5	5	5
Wrap angle(degree)	40.9	105.4	32.1	57.7	0.6–78.5	180	90

TABLE II
Cable–Pulley LuGre Parameters

σ_0	σ_1	σ_2	μ_c	μ_s	v_s	f_d
1e6	1000	500	0.15	0.20	5e-2 m/s	0.01

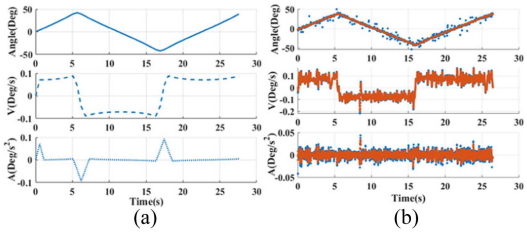

Fig. 11. (a) Joint simulation movement. (b) Real joint movement.

shown in Table II. Based on the aforementioned configuration, the joint motion simulation parameters are set to be consistent with the actual joint motion process, as shown in Fig. 11.

Two sets of experiments are conducted, each involving distinct preload forces. The preload is accurately measured using an end tension sensor while the system remains stationary. Specifically:

1) first set: preload forces of $T_{\text{up}} = 23.52$ N (upper cable) and $T_{\text{down}} = 6.66$ N (lower cable);
2) second set: preload forces of $T_{\text{up}} = 36.85$ N (upper cable) and $T_{\text{down}} = 26.26$ N (lower cable).

The original experimental data are fitted using the MATLAB *Smoothdata* function. To ensure a consistent benchmark, we introduce the sliding friction influence factor $\rho = 0.2$. Finally, we plot the parameter curves with respect to time and angle for a comprehensive comparison between the experimental and simulated results.

B. Validation of Cable Element Tension

The terminal cable element in our system is directly linked to a tension sensor, allowing for a precise measurement of cable tension. As depicted in Fig. 11, the tension sensor captures the actual scatter plot alongside its corresponding fitted curve. Simultaneously, a simulation curve represents the cable tension throughout the movement process. Remarkably, the simulation curve closely aligns with the actual measured fitting curve, demonstrating a high level of consistency.

Throughout a complete movement cycle, we have the following.

1) *Upper cable tension:* Initially, the upper cable tension gradually increases, followed by a subsequent decrease. Upon reversing the movement direction, there is a sudden upward tension shift, succeeded by a gradual increase and

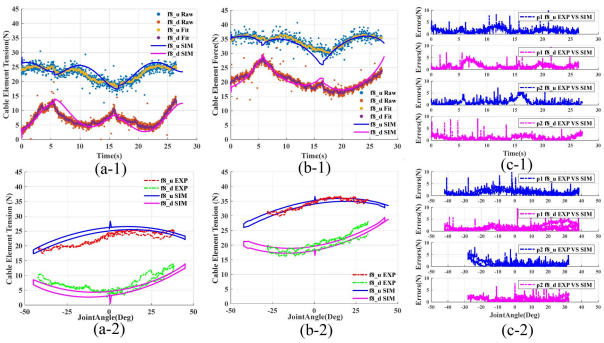

Fig. 12. Eighth cable element tension over time and angle with different preloads. (a) First set of preloads. (b) Second set of preloads. (c) Errors of simulation data and experimental results.

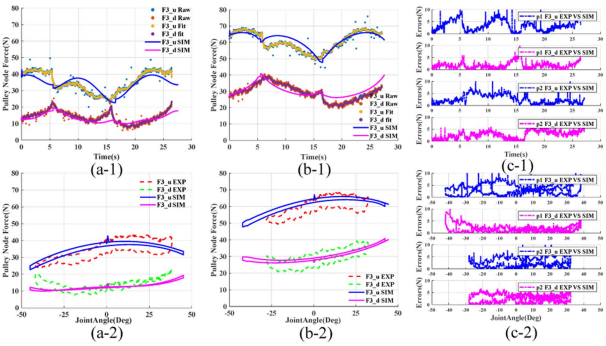

Fig. 13. Third pulley nodal force over time and angle with different preloads. (a) First set of preloads. (b) Second set of preloads. (c) Errors of simulation data and experimental results.

subsequent decrease. This tension profile resembles an overall "M" curve.

2) *Lower cable tension:* Conversely, the lower cable tension exhibits an inverted pattern, forming a distinct "W" curve.

Based on graphical analysis, under the first set of preload forces, the average force error is 1.34 N, with an average relative error rate of 13.65%. Under the second set of preload forces, the average force error is 1.10 N, with an average relative error rate of 4.44%. The error comparison charts in Fig. 12(c-1) and (c-2) show that discrepancies between simulation and experimental results are predominantly observed at three critical points: when the joint angle reaches its maximum and minimum limits, and when the maximum differential tension between the upper and lower cables is achieved. At these positions, abrupt changes in force and velocity occur, leading to increased errors. These errors can be mitigated by ensuring smooth transitions and controlled reversals in joint velocity. Furthermore, for the terminal cable element, the hysteresis effect induced by joint reciprocation is minimal, resulting in a strong correlation between the experimental and simulation curves throughout the entire process.

C. Validation of Pulley Node Force

The nodal force exerted on the third pulley is derived from the tension in adjacent cable elements, resulting in an overall tension that surpasses that of a solitary cable. Fig. 13 depicts simulation curves that are well aligned with the empirical data from the tension sensor, demonstrating a high degree of consistency in both quantitative values and the trend of changes. In contrast to the tension discrepancies observed with end cable actuation, the difference between symmetrical nodal forces becomes more pronounced as the preload force increases.

From the graphical evaluation, the average force error under the first set of preload forces is 2.58 N, with an average relative error of 11.86%, and under the second set of preload forces, the average force error is 2.68 N, with an average relative error of 6.74%. As shown in Fig. 13(c-1) and (c-2), the error exhibits periodic variation throughout the motion, indicating that the hysteresis effect on the nodal force is pronounced due to the cumulative influence of the forward cable elements and nodes. Specific deviations, particularly during abrupt directional changes at the joint, lead to significant fluctuations in cable element tension and nodal force. The most considerable tension error occurs during steering movements, likely due to minor jamming within the cable system, causing rapid tension release during reverse motion. In addition, the abrupt tension variation in the nodal force depicted in Fig. 13 exceeds that of the terminal cable element in Fig. 12. This discrepancy arises because the second node, being closer to the motor, experiences a swift tension switch upon a shift in the motor's rotational direction, which immediately affects the third node. In contrast, the transmission to the terminal cable is delayed and reduced in magnitude due to frictional effects.

D. Validation of the Friction Model

The proposed node tension model reveals that when the node force at any given node and the cable element tension are known, the parameters of other nodes and elements can be iteratively determined. In our simulation, a fixed value of ρ was employed, yielding results consistent with the actual data trends. Consequently, assuming that the sliding friction coefficient ρ for the pulley cable remains unknown, we can obtain the sliding friction coefficient under varying preloads through parameter identification. We define the residual of the objective function as follows:

$$\text{Res} = \sum (F3\_\text{cal} - F3\_\text{exp})^2. \tag{44}$$

$F3\_\text{cal}$ represents the third nodal force derived via iterative computation from f8, while $F3\_\text{exp}$ denotes the force ascertained through experimental measurement. The MATLAB function *fminbnd* was employed to ascertain the minimal value of a univariate function within a prescribed interval. The optimization process yielded coefficients of $\rho_{\text{up}} = 0.1114$ and $\rho_{\text{down}} = 0.3920$ under the first preload force group, and $\rho_{\text{up}} = 0.1100$ and $\rho_{\text{down}} = 0.1315$ under the second preload group. Incorporating these empirically determined sliding friction coefficients into the nodal tension distribution model facilitates the computation of the cable–pulley frictional forces under the actual parameters discerned.

Fig. 14 illustrates the correlation between frictional variation and the third node (corresponding to the second pulley) in relation to the cable. By substituting the empirically identified value of ρ into the nodal element model, the frictional force for the second pulley is derived. The observed variations closely mirror

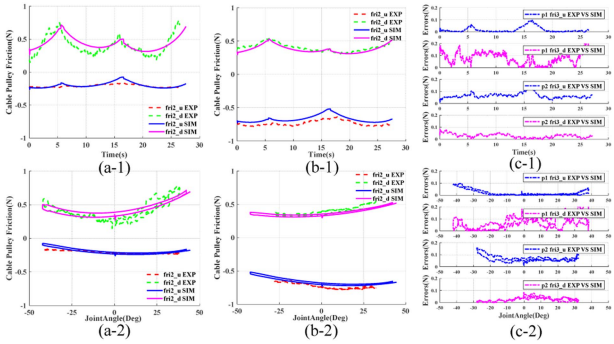

Fig. 14. Second cable–pulley friction over time and angle with different preloads. (a) First set of preloads. (b) Second set of preloads. (c) Errors of simulation data and experimental results.

empirical outcomes, confirming that different preload configurations significantly influence the system's sliding friction factor, ρ. As shown in Fig. 14(c-1) and (c-2), after substituting the identified ρ, the error remains within a small range, although it is still concentrated at the joint limit positions. According to the graphical assessment, the average force error under the first set of preload forces is 0.048 N, with an average relative error of 15.78%. Under the second set of preload forces, the average force error is 0.039 N, with an average relative error of 13.19%.

A substantial preload force ensures consistent cable tension, precluding slackness and predominantly inducing rolling friction, which results in relatively uniform changes in frictional force. Conversely, a minimal preload force increases the propensity for cable slackness and slippage between the cable and the pulley, with sliding friction prevailing and leading to marked fluctuations in frictional force, thereby impacting the operational stability of the system. Consequently, sustaining an optimal preload force within the cable's tensile strength threshold is imperative not only for diminishing system hysteresis and enhancing joint actuation efficacy but also for ensuring operational stability.

E. Discussion of the Proposed Model

Traditional finite-element methods discretize the cable into nodes, requiring the consideration of both the number of pulleys and the discretization points along the cable [11], leading to substantial computational demands, particularly for complex cable-driven systems. In addition, when using the classical Euler friction model [15], the tension transmission coefficient between nodes remains constant across varying preload forces and cable velocities, introducing significant errors in tension and nodal force calculations. Furthermore, most conventional models only address systems where pulleys are fixed [19], maintaining constant distances between nodes, which fails to account for the macro-length variations in more intricate systems, such as those involving rolling joints.

Unlike these traditional approaches, our proposed approach models the pulley as natural node within continuous cables, significantly reducing the number of finite-element nodes and enhancing computational efficiency. While previous models typically focus on single-cable closed-loop systems and concentrate nonlinear factors like friction at drive and joint pulleys [18], our model iteratively accounts for the effects of all pulleys and cables, accommodating varying preload forces across multiple independent cable systems. Unlike conventional models, which often overlook simultaneous cable sliding friction and bearing rolling friction [16], [19], [27], our extended LuGre model incorporates these factors into pulley–cable line contact scenarios. This approach more accurately captures dynamic changes in the system, thereby improving the overall accuracy of the results.

VI. Conclusion

This study designed a new type of cable-driven rolling joint and proposed a new node element tension distribution model, which greatly facilitates the analysis and solution of complex cable-driven systems. This model ingeniously distills complex pulley–cable assemblies into an intelligible array of nodes and elements, meticulously considering the diverse influences of preload forces and frictional dynamics. It employs an iterative approach to infer the conditions of indeterminate node elements based on established parameters. Our thorough investigation, which integrates dynamic sliding and rolling friction as per the LuGre model, has disclosed a pronounced impact of sliding friction on the system's efficacy in force transmission. The establishment of a rolling joint experimental platform has corroborated the model's precision, underscoring its prognostic value, especially in assessing the influence of preload force on system tension. The findings elucidate a direct correlation between heightened preload force and a reduced necessity for driving force in joint actuation.

The model is an invaluable tool for assessing cables and pulleys in space-constrained systems where tension sensors cannot be installed. Although the current model relies on initial preload input, future developments will allow for the direct mapping of the system's initial tension using cable stiffness and spring deflection, eliminating the need for tension sensors. However, it is crucial to recognize potential discrepancies due to the static nature of friction model parameters compared to real-world dynamics. Transient phenomena, such as changes in joint direction, may also cause sudden shifts in cable tension and nodal forces, diverging from the model's predictions. The model can be adapted to various robotic systems, including those used in space exploration, where compact and reliable mechanisms are critical. It also holds potential in biomechanics, prosthetics, and bioinspired design, where precise force transmission is essential. Future work will aim to further improve model accuracy, perform preload identification, and address challenges such as transient frictional effects. Expanding its scope across interdisciplinary applications will advance mechatronics and provide valuable insights for various scientific and engineering fields.

Appendix

Based on the simplified pulley node and cable element model in this article, the stiffness matrix coefficients between the node force and the initial preload force matrix and the node displacement and the pulley motion matrix are obtained through sequential iterations

$$[\mathbf{K}] = \begin{bmatrix} \mathbf{K}_{\Delta\Delta} & \mathbf{K}_{\Delta s} \\ \mathbf{K}_{s\Delta} & \mathbf{K}_{ss} \end{bmatrix}.$$

The specific expression is as follows:

$$[\mathbf{K}_{\Delta\Delta}] = \begin{bmatrix} \mathbf{k}_{\Delta\Delta}^{(1)} & -\mathbf{k}_{\Delta\Delta}^{(1)} & & & & & \\ -\mathbf{k}_{\Delta\Delta}^{(1)} & \mathbf{k}_{\Delta\Delta}^{(1)}+\mathbf{k}_{\Delta\Delta}^{(2)} & \dots & & \mathbf{0} & & \\ & -\mathbf{k}_{\Delta\Delta}^{(2)} & \dots & -\mathbf{k}_{\Delta\Delta}^{(i-1)} & & & \\ & & \dots & \mathbf{k}_{\Delta\Delta}^{(i-1)}+\mathbf{k}_{\Delta\Delta}^{(i)} & \dots & & \\ & & & -\mathbf{k}_{\Delta\Delta}^{(i)} & \dots & -\mathbf{k}_{\Delta\Delta}^{(n-1)} & \\ & \mathbf{0} & & & \dots & \mathbf{k}_{\Delta\Delta}^{(n-1)}+\mathbf{k}_{\Delta\Delta}^{(n)} & -\mathbf{k}_{\Delta\Delta}^{(n)} \\ & & & & & -\mathbf{k}_{\Delta\Delta}^{(n)} & \mathbf{k}_{\Delta\Delta}^{(n)} \end{bmatrix}$$

$$[\mathbf{K}_{\Delta s}] = \begin{bmatrix} -\mathbf{k}_{\Delta s}^{(1)} & & & & & & \\ \mathbf{k}_{\Delta s}^{(1)}+\mathbf{k}_{\Delta s}^{(2)} & -\mathbf{k}_{\Delta s}^{(2)} & & & \mathbf{0} & & \\ \mathbf{k}_{\Delta s}^{(2)} & \mathbf{k}_{\Delta s}^{(2)}+\mathbf{k}_{\Delta s}^{(3)} & \dots & -\mathbf{k}_{\Delta s}^{(i-1)} & & & \\ & -\mathbf{k}_{\Delta s}^{(3)} & \dots & \mathbf{k}_{\Delta s}^{(i-1)}+\mathbf{k}_{\Delta s}^{(i)} & \dots & -\mathbf{k}_{\Delta s}^{(n-2)} & \\ & & \dots & -\mathbf{k}_{\Delta s}^{(i)} & \dots & \mathbf{k}_{\Delta s}^{(n-2)}+\mathbf{k}_{\Delta s}^{(n-1)} & -\mathbf{k}_{\Delta s}^{(n-1)} \\ & \mathbf{0} & & & \dots & -\mathbf{k}_{\Delta s}^{(n-1)} & \mathbf{k}_{\Delta s}^{(n-1)}+\mathbf{k}_{\Delta s}^{(n)} \\ & & & & & & -\mathbf{k}_{\Delta s}^{(n)} \end{bmatrix}_{3n\times(n-2)}$$

$$[\mathbf{K}_{s\Delta}] = \begin{bmatrix} -\eta_2\mathbf{k}_{s\Delta}^{(1)} & \eta_2\mathbf{k}_{s\Delta}^{(1)}+\mathbf{k}_{s\Delta}^{(2)} & -\mathbf{k}_{s\Delta}^{(2)} & & & \\ & -\eta_3\mathbf{k}_{s\Delta}^{(2)} & \eta_3\mathbf{k}_{s\Delta}^{(2)}+\mathbf{k}_{s\Delta}^{(3)} & -\mathbf{k}_{s\Delta}^{(3)} & & \mathbf{0} \\ & & \dots & \dots & \dots & \\ & & -\eta_i\mathbf{k}_{s\Delta}^{(i-1)} & \eta_i\mathbf{k}_{s\Delta}^{(i-1)}+\mathbf{k}_{s\Delta}^{(i)} & -\mathbf{k}_{s\Delta}^{(i)} & \\ & & & \dots & \dots & \dots \\ & \mathbf{0} & & -\eta_{n-2}\mathbf{k}_{s\Delta}^{(n-3)} & \eta_{n-2}\mathbf{k}_{s\Delta}^{(n-3)}+\mathbf{k}_{s\Delta}^{(n-2)} & -\mathbf{k}_{s\Delta}^{(n-2)} \\ & & & & -\eta_{n-1}\mathbf{k}_{s\Delta}^{(n-2)} & \eta_{n-1}\mathbf{k}_{s\Delta}^{(n-2)}+\mathbf{k}_{s\Delta}^{(n-1)} & -\mathbf{k}_{s\Delta}^{(n-1)} \end{bmatrix}_{(n-2)\times 3n}$$

$$[\mathbf{K}_{ss}] = \begin{bmatrix} \eta_2 k^{(1)}+k^{(2)} & -k^{(2)} & & & & \\ -\eta_3 k^{(2)} & \eta_2 k^{(2)}+k^{(3)} & -k^{(3)} & & \mathbf{0} & \\ & \dots & \dots & \dots & & \\ & & -\eta_i k^{(i-1)} & \eta_i k^{(i-1)}+k^{(i)} & -k^{(i)} & \\ & & \dots & \dots & \dots & \\ & \mathbf{0} & & & -\eta_{n-2}k^{(n-3)} & \eta_{n-2}k^{(n-3)}+k^{(n-2)} & -k^{(n-2)} \\ & & & & & -\eta_{n-1}k^{(n-2)} & \eta_{n-1}k^{(n-2)}+k^{(n-1)} \end{bmatrix}_{(n-2)\times(n-2)}.$$

REFERENCES

[1] X. Zheng, T. Yang, Z. Chen, X. Wang, B. Liang, and Q. Liao, "ALE formulation for dynamic modeling and simulation of cable-driven mechanisms considering stick–slip frictions," *Mech. Syst. Signal Process.*, vol. 168, Apr. 2022, Art. no. 108633, doi: 10.1016/j.ymssp.2021.108633.

[2] W. Li, X. Huang, L. Yan, H. Cheng, B. Liang, and W. Xu, "Force sensing and compliance control for a cable-driven redundant manipulator," *IEEE/ASME Trans. Mechatron.*, vol. 29, no. 1, pp. 777–788, Feb. 2024, doi: 10.1109/TMECH.2023.3263922.

[3] Y. Wang, W. Li, S. Togo, H. Yokoi, and Y. Jiang, "Survey on main drive methods used in humanoid robotic upper limbs," *Cyborg Bionic Syst.*, vol. 2021, pp. 1–12, 2021, doi: 10.34133/2021/9817487.

[4] Y.-J. Kim, "Anthropomorphic low-inertia high-stiffness manipulator for high-speed safe interaction," *IEEE Trans. Robot.*, vol. 33, no. 6, pp. 1358–1374, Dec. 2017, doi: 10.1109/TRO.2017.2732354.

[5] Y. Huang, Y. Chen, X. Zhang, H. Zhang, C. Song, and J. Ota, "A novel cable-driven 7-DOF anthropomorphic manipulator," *IEEE/ASME Trans. Mechatron.*, vol. 26, no. 4, pp. 2174–2185, Aug. 2021, doi: 10.1109/TMECH.2020.3033309.

[6] S. Pang, W. Shang, F. Zhang, B. Zhang, and S. Cong, "Design and stiffness analysis of a novel 7-DOF cable-driven manipulator," *IEEE Robot. Automat. Lett.*, vol. 7, no. 2, pp. 2811–2818, Apr. 2022, doi: 10.1109/LRA.2022.3144776.

[7] S. Pang et al., "Stiffness optimization of cable-driven humanoid manipulators," *IEEE/ASME Trans. Mechatron.*, early access, doi: 10.1109/TMECH.2024.3367926.

[8] N. Aswal, S. Sen, and L. Mevel, "Estimation of local failure in tensegrity using interacting particle-ensemble Kalman filter," *Mech. Syst. Signal Process.*, vol. 160, Nov. 2021, Art. no. 107824, doi: 10.1016/j.ymssp.2021.107824.

[9] S. N. Kosari, S. Ramadurai, H. J. Chizeck, and B. Hannaford, "Control and tension estimation of a cable driven mechanism under different tensions," in *Proc. ASME Int. Des. Eng. Tech. Conf. Comput. Inf. Eng. Conf.*, Feb. 2014, Art. no. DETC2013-13548. doi: 10.1115/DETC2013-13548.

[10] H. Yuan, E. Courteille, and D. Deblaise, "Static and dynamic stiffness analyses of cable-driven parallel robots with non-negligible cable mass and elasticity," *Mech. Mach. Theory*, vol. 85, pp. 64–81, Mar. 2015, doi: 10.1016/j.mechmachtheory.2014.10.010.

[11] Z. Qi, J. Wang, and G. Wang, "An efficient model for dynamic analysis and simulation of cable-pulley systems with time-varying cable lengths," *Mech. Mach. Theory*, vol. 116, pp. 383–403, Oct. 2017, doi: 10.1016/j.mechmachtheory.2017.06.009.

[12] Y. Peng, Y. Wei, and M. Zhou, "Efficient modeling of cable-pulley system with friction based on arbitrary-Lagrangian-Eulerian approach," *Appl. Math. Mech.*, vol. 38, no. 12, pp. 1785–1802, Dec. 2017, doi: 10.1007/s10483-017-2284-8.

[13] Z. Zhang, G. Xie, Z. Shao, and C. Gosselin, "Kinematic calibration of cable-driven parallel robots considering the pulley kinematics," *Mech. Mach. Theory*, vol. 169, 2022, Art. no. 104648, doi: 10.1016/j.mechmachtheory.2021.104648.

[14] Z. Zhou, X. Zheng, Z. Chen, X. Wang, B. Liang, and Q. Wang, "Dynamics modeling and analysis of cable-driven segmented manipulator considering friction effects," *Mech. Mach. Theory*, vol. 169, Mar. 2022, Art. no. 104633, doi: 10.1016/j.mechmachtheory.2021.104633.

[15] O. Baser and E. I. Konukseven, "Theoretical and experimental determination of capstan drive slip error," *Mech. Mach. Theory*, vol. 45, no. 6, pp. 815–827, Jun. 2010, doi: 10.1016/j.mechmachtheory.2009.10.013.

[16] F. Ju and Y. S. Choo, "Super element approach to cable passing through multiple pulleys," *Int. J. Solids Struct.*, vol. 42, no. 11/12, pp. 3533–3547, 2005, doi: 10.1016/j.ijsolstr.2004.10.014.

[17] F. Grashof, "Theoretische maschinenlehre," *Nature*, vol. 7, no. 160, Nov. 1872, Art. no. 45, doi: 10.1038/007045b0.

[18] Y. Zhang, L. He, and C. Wu, "The effect of preload force on damping in tendon-driven manipulator," *Ind. Robot: Int. J. Robot. Res. Appl.*, vol. 48, no. 3, pp. 454–462, 2021, doi: 10.1108/IR-10-2020-0232.

[19] Y. Cho, B. Kang, C. Park, and J. Cheong, "Kinematics of elastic tendons for tendon-driven manipulators with transmission friction," *IEEE/ASME Trans. Mechatron.*, vol. 27, no. 1, pp. 202–213, Feb. 2022, doi: 10.1109/TMECH.2021.3060424.

[20] E. Pennestrì, V. Rossi, P. Salvini, and P. P. Valentini, "Review and comparison of dry friction force models," *Nonlinear Dyn.*, vol. 83, no. 4, pp. 1785–1801, Mar. 2016, doi: 10.1007/s11071-015-2485-3.

[21] K. Johanastrom and C. Canudas-de-Wit, "Revisiting the LuGre friction model," *IEEE Control Syst. Mag.*, vol. 28, no. 6, pp. 101–114, Dec. 2008, doi: 10.1109/MCS.2008.929425.

[22] J.-Y. Kuan, K. A. Pasch, and H. M. Herr, "A high-performance cable-drive module for the development of wearable devices," *IEEE/ASME Trans. Mechatron.*, vol. 23, no. 3, pp. 1238–1248, Jun. 2018, doi: 10.1109/TMECH.2018.2822764.

[23] K. Yang et al., "Cable tension analysis oriented the enhanced stiffness of a 3-DOF joint module of a modular cable-driven human-like robotic arm," *Appl. Sci.*, vol. 10, no. 24, 2020, Art. no. 8871, doi: 10.3390/app10248871.

[24] Z. Kan, H. Peng, and B. Chen, "A simple linear complementarity approach for sliding cable modeling considering friction," *Mech. Syst. Signal Process.*, vol. 130, pp. 293–314, Sep. 2019, doi: 10.1016/j.ymssp.2019.05.012.

[25] Q. Chen, "Mechanism design and tension analysis of a cable-driven humanoid-arm manipulator with joint angle feedback," *J. Mech. Eng.*, vol. 46, no. 13, 2010, Art. no. 83, doi: 10.3901/JME.2010.13.083.

[26] D. B. Camarillo, C. F. Milne, C. R. Carlson, M. R. Zinn, and J. K. Salisbury, "Mechanics modeling of tendon-driven continuum manipulators," *IEEE Trans. Robot.*, vol. 24, no. 6, pp. 1262–1273, Dec. 2008, doi: 10.1109/TRO.2008.2002311.

[27] Y. Li, Y. Liu, D. Meng, X. Wang, and B. Liang, "Modeling and experimental verification of a cable-constrained synchronous rotating mechanism considering friction effect," *IEEE Robot. Automat. Lett.*, vol. 5, no. 4, pp. 5464–5471, Oct. 2020, doi: 10.1109/LRA.2020.3007418.

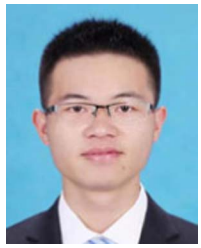

Song Zeng received the B.S. and M.S. degrees in mechanical engineering, in 2014 and 2021, respectively, from Beihang University, Beijing, China, where he is currently working toward the Ph.D. degree in mechanical engineering with the School of Automation Science and Electrical Engineering.

His research interests include mechanical design, cable-driven robots, and cable precision modeling.

Yixin Zhang received the B.Eng., M.Eng., and Ph.D. degrees in mechatronics engineering from Beihang University, Beijing, China, in 2013, 2017, and 2021, respectively.

He is currently a Postdoctoral Research Fellow with the School of Automation Science and Electrical Engineering, Beihang University. His research interests include biomechatronics, intelligent robots, and biomimetic propulsive mechanism.

Shaoping Wang received the B.Eng., M.Eng., and Ph.D. degrees in mechatronics engineering from Beihang University, Beijing, China, in 1988, 1991, and 1994, respectively.

Since 1994, she has been with the School of Automation Science and Electrical Engineering, Beihang University, where she became a Professor in 2000. Her research interests include engineering reliability, biomechatronics control, and biomechatronics.

Dr. Wang was honored as a Changjiang Scholar Professor by the Ministry of Education of China in 2013.

Giorgio Guglieri is a full professor of flight mechanics at Politecnico di Torino, and he is the Head of Department of Mechanical and Aerospace Engineering, Politecnico di Torino. He received his M.Sc. degree in mechanical engineering from Politecnico di Torino, in 1989. He carries out teaching activities in the Aerospace Engineering degree program of the Politecnico di Torino, as responsible of the courses in Introduction to Flight Mechanics and Helicopter Flight Mechanics. He is a member of the steering board of the Ph.D. Program in Aerospace Engineering. He is a senior member of AIAA (American Institute of Aeronautics and Astronautics) and AHS (American Helicopter Society). He is involved in research activities in the following fields: flight mechanics of fixed and rotary wing aircraft, flight simulation, design of human-machine interfaces for robotics, development and testing of unmanned aerial systems, planning and mission control for autonomous systems, design of guidance, control and navigation systems for aircraft and spacecraft. As part of his research activities, he collaborates with academic institutions, research centers, networks and companies, both in Italy and abroad.

Stefano Primatesta received the B.S. degree in electronic engineering, the M.Sc. degree in mechatronic engineering, and the Ph.D. degree in computer and control engineering from the Politecnico di Torino, Torino, Italy, in 2011, 2014, and 2019, respectively.

He is currently an Assistant Professor with the Department of Mechanical and Aerospace Engineering, Politecnico di Torino. His field of research is the use of remotely piloted aircraft systems in urban environments including virtual modeling and multidimensional risk analysis. His research interests include autonomous navigation and service robotics, with applications on unmanned aerial vehicles and unmanned ground vehicles.

Wenjie Wu received the B.S. degree in automation from the Civil Aviation University of China, Tianjin, China, in 2019, and the M.S. degree in power engineering from Harbin Engineering University, Harbin, China, in 2022. He is currently working toward the Ph.D. degree in navigation guidance and control with the School of Automation Science and Electrical Engineering, Beihang University, Beijing, China.

His research interests include sliding-mode control, fuzzy systems, robust control, and adaptive control.